European Journal of Mechanics / B Fluids 74 (2019) 167–179

Contents lists available at ScienceDirect

European Journal of Mechanics / B Fluids

journal homepage: www.elsevier.com/locate/ejmflu

Electrohydrodynamics in leaky dielectric fluids using lattice Boltzmann method

Rattandeep Singh, Supreet Singh Bahga, Amit Gupta *

Department of Mechanical Engineering, Indian Institute of Technology Delhi, Hauz Khas, New Delhi 110016, India

ARTICLE INFO

Article history:
Received 21 May 2018
Received in revised form 19 September 2018
Accepted 14 November 2018
Available online 26 November 2018

Keywords:
Leaky dielectric model
Lattice Boltzmann method
Electrohydrodynamics
Multi-component model

ABSTRACT

The application of an electric field on a multi-component leaky dielectric fluid system leads to an electric stress at the fluid–fluid interface. To capture the effect of these electric stresses, we report a new method to couple the electrostatics and hydrodynamics of leaky dielectric fluids within the framework of the lattice Boltzmann method. The developed methodology relies on obtaining time invariant solution to the equation governing the divergence of current density in the flow domain using a time marching lattice Boltzmann equation or through a finite-difference formulation. The coupling between the low spurious velocity hydrodynamics model and the leaky dielectric counterpart is also illustrated through the use of three case studies involving interaction of single or multiple droplets suspended in an outer fluid under the action of an external electric field. The results obtained from the developed methodology are shown to be in excellent agreement with earlier published analytical and numerical results. Further, the numerical experiments demonstrate that the developed methodology is applicable for both steady- and time-dependent flows.

© 2018 Elsevier Masson SAS. All rights reserved.

1. Introduction

Electrohydrodynamics (EHD) deals with the study of fluid motion induced by an electric field [1]. In the presence of an electric field, the free charge carriers present in a fluid gives rise to electric conduction and the bound charges give rise to polarization [2]. On applying a DC electric field to a multiphase system, charges because of polarization appears at the interface of each phase. Also, the free charge carriers present in each fluid migrate to the fluid–fluid interface. The accumulation of charge in the presence of electric field leads to an electric stress at the interface [1], thereby influencing the fluid flow. This manipulation of fluid motion using an electric field has found applications in a variety of multiphase flows, such as droplet breakup [3], coalescence of droplets and solvent extraction [4], and electrospraying [5].

The EHD flows in multiphase systems depend strongly on the conductivity and permittivity of the fluids. For example, a droplet of perfect conducting or perfect dielectric liquid immersed in another immiscible perfect insulating liquid subjected to electric field attains a prolate shape by elongating along the direction of electric field with no net fluid motion observed in the equilibrium state [1,6]. In contrast, a weakly conducting drop (leaky dielectric fluid) suspended in another immiscible leaky dielectric fluid elongates either along or perpendicular to the direction of electric field [7]. Such effects of permittivity and conductivity on EHD flows of multiphase fluids were first examined by Taylor [8] who recognized that leaky dielectric fluids can transmit free charge to the fluid–fluid interface. This free charge leads to an electric stress along both the normal and the tangential direction to the fluid–fluid interface. The tangential component of the electric stress drives fluid into motion thereby generating a hydrodynamic stress at the interface. This EHD theory proposed by Taylor [8] is referred to as the leaky dielectric model [1].

The response of leaky dielectric fluids under the influence of electric field can be used in many processes such as droplet formation [9], breakup [3] and coalescence [10]. An efficient control of these applications require an in-depth understanding of the interaction of electric field with leaky dielectric fluids. Though the EHD flows of leaky dielectric fluids have been extensively studied both experimentally and analytically [1,3,11–15], due to the complicated electro-mechanical coupling between electric field and the fluids, analytical studies employ various simplifying assumptions. Thus, numerical simulations are required to accurately model the EHD of leaky dielectric fluids. Based on the approach used to define the fluid–fluid interface, numerical methods of the EHD flows can be categorized as: (i) front tracking method [16], (ii) level set method [17], (iii) volume of fluids [18–21] and (iv) immersed boundary and immersed interface method [22]. However, all these interface capturing techniques are based on solving a separate equation for tracking the fluid–fluid interface along with the Navier–Stokes equation. The boundary element method

* Corresponding author.
E-mail address: agupta@mech.iitd.ac.in (A. Gupta).

https://doi.org/10.1016/j.euromechflu.2018.11.011
0997-7546/© 2018 Elsevier Masson SAS. All rights reserved.

is another approach to simulate EHD flows [6,23,24]. However, its applicability is limited to inviscid and Stokes flow problems.

The lattice Boltzmann method (LBM) has emerged as a powerful tool to simulate fluid flow in applications involving interfacial dynamics [25,26]. As compared to the conventional Navier–Stokes' solvers, some of the salient features of lattice Boltzmann method include (i) solution of a linear partial differential equation which is relatively easier than the non-linear Navier–Stokes equation, (ii) no special treatment required to calculate static pressure, while in Navier–Stokes equation static pressure is determined by solving Poisson's equation, and (iii) matrix inversions are not required in lattice Boltzmann method as the governing equations are local in nature, thus making it ideal for parallelization [26]. While lattice Boltzmann method is widely used for simulating multi-component flows, its development for EHD flows has received little attention. Zhang and Kwok [27] first used lattice Boltzmann method to study droplet deformation in the presence of an electric field by coupling the pseudo-potential method for multiphase simulations [28] and lattice Boltzmann equation for computing electric potential [29]. EHD effects on a droplet suspended in another immiscible fluid were also analyzed by Li et al. [30] by coupling the pseudo-potential method [28] with the electrostatic model. However, one of the major limitations of the pseudo-potential method [28] is that it renders high spurious velocities at the fluid–fluid interface [31] which can only be reduced by using higher-order discretization. Moreover, the pseudo-potential model [28] is not the favored option for simulating fluid flow problems where Reynolds number is of $O(1)$ or less [31]. Further, the applicability of the previously developed models [27,30] was limited to two-dimensional steady flows only.

In this paper, a low spurious current lattice Boltzmann model for accurate numerical simulations of EHD flows in multi-component fluids is presented. The proposed numerical framework is applicable to both two and three-dimensional fluid system which can be approximated as leaky dielectric fluids. The coupling of the leaky dielectric model with the lattice Boltzmann method is achieved by incorporating a body force due to the electric field directly at the fluid–fluid interface. The proposed method is validated with earlier reported theoretical and numerical studies to highlight the capability of the developed model to accurately simulate steady and unsteady EHD flows.

2. Mathematical model

The governing equations for fluid flow in the presence of an electric field are called EHD equations, and can be expressed as

$$\nabla \cdot (\rho \mathbf{u}) = 0, \tag{1}$$

$$\frac{\partial (\rho \mathbf{u})}{\partial t} + \mathbf{u} \cdot \nabla(\rho \mathbf{u}) = -\nabla p + \mu \nabla^2 \mathbf{u} + \gamma \kappa \mathbf{n} \delta + \nabla \cdot \underline{\mathbf{T}}^E, \tag{2}$$

where ρ, $\mathbf{u}$, p and μ are the fluid density, velocity field, pressure and dynamic viscosity, respectively. γ is the interfacial tension, κ is the local curvature of the interface and δ is the Dirac-delta function. $\underline{\mathbf{T}}^E$ is the Maxwell stress tensor acting at the fluid–fluid interface. The Maxwell stress arises due to the discontinuity of the electrical properties at the fluid interface and is expressed as [32]

$$\underline{\mathbf{T}}^E = \varepsilon(\mathbf{E}\mathbf{E} - \frac{1}{2}E^2\underline{\mathbf{I}}). \tag{3}$$

Here, ε is the dielectric permittivity, $\mathbf{E}$ represents the electric field and $\underline{\mathbf{I}}$ is the identity tensor. In Eq. (3), the electrostriction force term has been neglected. The governing equations required for the calculation of $\underline{\mathbf{T}}^E$ are discussed as follows.

The electric field is related to the conductivity σ and free charge density ρ_f by the charge conservation equation [33]

$$\frac{\partial \rho_f}{\partial t} + \nabla \cdot (\rho_f \mathbf{u} + \sigma \mathbf{E}) = 0, \tag{4}$$

where $\rho_f = \nabla \cdot (\varepsilon \mathbf{E})$. Since charge relaxation time scale in electrostatics is assumed to be very small and charges are considered to be static [34], Eq. (4) becomes

$$\nabla \cdot (\sigma \mathbf{E}) = 0, \tag{5}$$

where

$$\nabla \times \mathbf{E} = 0. \tag{6}$$

The Eqs. (1)–(3) and (5) are solved simultaneously to compute the flow of leaky dielectric fluids. The numerical method developed to perform these simulations is discussed below.

2.1. Hydrodynamics of multi-component fluids

In this study, lattice Boltzmann method is used to simulate the hydrodynamics of fluids. The fundamental idea of the lattice Boltzmann method is to develop simplified kinetic models for macroscopic fluid flows, which includes the essential physics of mesoscopic processes. As the macroscopic dynamics of a fluid is the result of collective behavior of microscopic particles in the fluid, the macroscopic averaged properties obtained from such kinetic models obey the desired macroscopic equations [26].

The discretized form of the lattice Boltzmann equation along the direction "i" is given by

$$f_i(\mathbf{x} + \mathbf{e}_i \delta t, t + \delta t) = f_i(\mathbf{x}, t) + \Omega_i(f_i(\mathbf{x}, t)) + \Phi_i, \quad i = 0, 1, \ldots, N, \tag{7}$$

where

$$\Omega_i(f_i(\mathbf{x}, t)) = -\frac{f_i(\mathbf{x}, t) - f_i^{eq}(\mathbf{x}, t)}{\tau}. \tag{8}$$

Here, f_i is the particle distribution function, e_i is the microscopic velocity, Φ_i is the source term and N is the number of links at each lattice node. In Eq. (8), Ω_i is the linearized form of the collision operator with the single relaxation time, f_i^{eq} is the local equilibrium distribution function and τ is the dimensionless relaxation time. The local equilibrium distribution function f_i^{eq} along the direction "i" is expressed as

$$f_i^{eq} = w_i \rho \left[1 + \frac{\mathbf{e}_i \cdot \mathbf{u}}{c_s^2} + \frac{(\mathbf{e}_i \cdot \mathbf{u})^2}{2c_s^4} - \frac{\mathbf{u} \cdot \mathbf{u}}{2c_s^2}\right], \tag{9}$$

where ρ is the macroscopic density, $\mathbf{u}$ is the macroscopic velocity vector, c_s is the speed of sound in lattice units and w_i is the weight function. The D2Q9 and D3Q19 lattice model were employed for two-dimensional and three-dimensional simulations. For the D2Q9 model, the lattice velocity vectors are given as

$$\mathbf{e}_\alpha = \begin{cases} (0, 0), & \alpha = 0 \\ (\pm 1, 0), (0, \pm 1) & \alpha = 1, 2, 3, 4 \\ (\pm 1, \pm 1), (\pm 1, \pm 1) & \alpha = 5, 6, 7, 8, \end{cases} \tag{10}$$

and the weight functions are

$$w_i = \begin{cases} 4/9 & \text{for} \quad i = 0 \\ 1/9 & \text{for} \quad i = 1, \ldots, 4 \\ 1/36 & \text{for} \quad i = 5, \ldots, 8. \end{cases} \tag{11}$$

The lattice velocity vectors and the weight function for the D3Q19 lattice model are given as

$$\mathbf{e}_\alpha = \begin{cases} (0, 0, 0), & \alpha = 0 \\ (\pm 1, 0, 0), (0, \pm 1, 0), (0, 0, \pm 1) & \alpha = 1, \ldots, 6 \\ (\pm 1, \pm 1, 0), (\pm 1, 0, \pm 1), (0, \pm 1, \pm 1) & \alpha = 7, \ldots, 18, \end{cases}$$

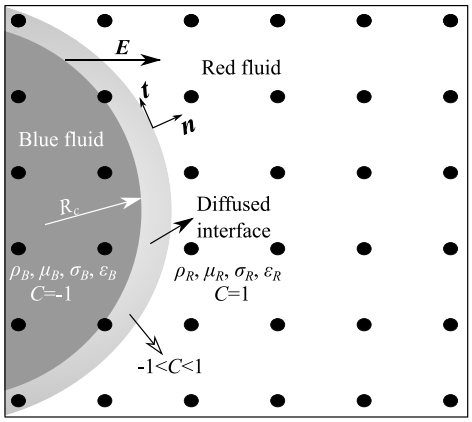

Fig. 1. Illustration of a diffused interface multi-component lattice Boltzmann method. The two fluids are represented by subscripts '*R*' and '*B*' and are separated by a diffused interface. The color distribution function, *C*, is defined based on the density of fluids. The value of *C* is fixed for each fluid and varies from −1 to 1 along the diffused interface.

(12)

and

$$w_i = \begin{cases} 1/3 & \text{for} \quad i = 0 \\ 1/18 & \text{for} \quad i = 1, \ldots, 6 \\ 1/36 & \text{for} \quad i = 7, \ldots, 18, \end{cases} \tag{13}$$

respectively.

Knowing the particle distribution f_i, the macroscopic density and momentum in the lattice Boltzmann method can be obtained as

$$\rho = \sum_i f_i = \sum_i f_i^{eq} \ , \ \ \rho \mathbf{u} = \sum_i f_i \mathbf{e}_i = \sum_i f_i^{eq} \mathbf{e}_i. \tag{14}$$

Chen and Doolen [26] have shown that using the Chapman–Enskog expansion together with Eq. (14), the differential form of the single relaxation time Boltzmann equation can be reduced to the Navier–Stokes equation in the low frequency and long wavelength limit. The pressure and kinematic viscosity can then be written as $p = c_s^2 \rho$ and $\nu = (\tau - 0.5) c_s^2 \delta t$.

Eq. (7) can be conveniently solved using a two step algorithm consisting of (i) collision, and (ii) streaming steps. During the collision step, the distribution function acquires the direction to stream to the neighboring node.

$$f_i^t(\mathbf{x}, t + \delta t) = f_i(\mathbf{x}, t) - \frac{1}{\tau}(f_i(\mathbf{x}, t) - f_i^{eq}(\mathbf{x}, t)) + \Phi_i(\mathbf{x}, t), \tag{15}$$

where f_i^t denotes the temporary distribution function. In the streaming step, the temporary distribution function f_i^t at the current lattice node overrides the value of the distribution function of the surrounding nodes

$$f_i(\mathbf{x} + \mathbf{e}_i \delta t, t + \delta t) = f_i^t(\mathbf{x}, t + \delta t). \tag{16}$$

On determining the distribution function the macroscopic properties of the fluid can be calculated using Eq. (14).

2.2. Coupled multicomponent-leaky dielectric model

To study electrohydrodynamics of multi-component leaky dielectric fluids with equal densities, we have developed a framework by which the electrodynamic and hydrodynamic models can be coupled within the lattice Boltzmann method. The hydrodynamic model of the developed framework involves the implementation of the color-fluid model of Gunstensen et al. [35] and incorporates the improvements made by Lishchuk et al. [36]. This modification in the original model (Gunstensen et al. [35]) facilitates the computation of flows where Reynolds number is of the $O(1)$ or less [31]. The hydrodynamic model has been applied to analyze the physics of rheology in emulsions [37], formation of droplets in cross-flow microfluidic device [38] and model the buoyant rise of single and multiple bubbles [39].

A schematic illustration of the multi-component model is shown in Fig. 1. A color code namely "red" and "blue" is used to identify the fluids. The red and the blue fluids are immiscible and are separated from each other by a diffused interface. The unit normal and tangential vectors at the diffused interface are represented by **n** and **t**, respectively. For each phase a particle distribution function is defined and are denoted by f_i^R and f_i^B, where superscripts "R" and "B" denote the red and blue fluids, respectively. The density of each phase is determined as

$$\rho_R(\mathbf{x}, t) = \sum_i f_i^R(\mathbf{x}, t), \tag{17}$$

$$\rho_B(\mathbf{x}, t) = \sum_i f_i^B(\mathbf{x}, t). \tag{18}$$

In the present multicomponent model, instead of a discontinuous jump, the fluid properties undergo a continuous variation across the fluid–fluid interface. To achieve this, a color function *C* based on the density of each fluid is defined, expressed as

$$C(\mathbf{x}, t) = \frac{\rho_R(\mathbf{x}, t) - \rho_B(\mathbf{x}, t)}{\rho_R(\mathbf{x}, t) + \rho_B(\mathbf{x}, t)}. \tag{19}$$

The value of *C* shows an insignificant variation in the pure phase and undergoes a smooth transition across the fluid–fluid interface thereby creating a diffused region separating the two immiscible fluids. The unit normal vector **n** to this diffused interface can be obtained using the gradient of the color function and is defined as

$$\mathbf{n} = -\frac{\nabla C}{|\nabla C|}. \tag{20}$$

This unit normal vector can be further used to determine the local curvature κ of the diffused interface, expressed as

$$\kappa = \frac{1}{R_c} = -\nabla_S \cdot \mathbf{n}, \tag{21}$$

where R_c is the local radius of curvature of the diffused interface, as shown in Fig. 1, and ∇_S is the surface gradient operator, given as

$$\nabla_S = (\underline{\mathbf{I}} - \mathbf{nn}) \cdot \nabla. \tag{22}$$

The hydrodynamics is modeled as follows. The red and blue fluids undergo collision operation (Eq. (15)) as a mixed fluid in which the particle distribution function $f_i^T(\mathbf{x}, t)$ is given as

$$f_i^T(\mathbf{x}, t) = f_i^R(\mathbf{x}, t) + f_i^B(\mathbf{x}, t), \tag{23}$$

with the relaxation time as

$$\tau(\mathbf{x}, t) = \frac{\tau_R \rho_R(\mathbf{x}, t) + \tau_B \rho_B(\mathbf{x}, t)}{\rho_R(\mathbf{x}, t) + \rho_B(\mathbf{x}, t)}. \tag{24}$$

Here τ_R and τ_B are the dimensionless relaxation times of the red and blue fluids, respectively. The source term incorporating the pressure force is augmented in the collision operator and is given as [40]

$$\Phi_I = w_i \left(1 - \frac{1}{2\tau}\right) \left[\frac{\mathbf{e}_i - \mathbf{u}}{c_s^2} + \frac{(\mathbf{e}_i \cdot \mathbf{u})}{c_s^4} \mathbf{e}_i\right] \cdot \mathbf{F}_I, \tag{25}$$

where $\mathbf{F}_I$ is defined as [36]

$$\mathbf{F}_I = -\frac{1}{2R_c} \gamma \nabla C. \tag{26}$$

Here $\mathbf{u}$ is the corrected velocity used in the calculation of f_i^{eq} and is given as

$$\mathbf{u} = \frac{1}{\rho}\left[\sum_i f_i \mathbf{e}_i + \frac{1}{2}\mathbf{F}_I\right]. \tag{27}$$

The computation of force term $\mathbf{F}_I$ using Eq. (26) significantly reduces the spurious velocities at the fluid–fluid interface [31,36].

To sharpen the interface and further reduce spurious velocities, a recoloring algorithm proposed by Latva-Kokko and Rothman [41] is incorporated. In this method, the post collision distributions of the red and blue fluids are computed as

$$f_{i,R}^{\ddagger} = \frac{\rho_R}{\rho_R+\rho_B} f_i + w_i \beta \frac{\rho_R \rho_B}{\rho_R+\rho_B}\mathbf{e}_i \cdot \mathbf{n}, \tag{28}$$

$$f_{i,B}^{\ddagger} = \frac{\rho_B}{\rho_R+\rho_B} f_i - w_i \beta \frac{\rho_R \rho_B}{\rho_R+\rho_B}\mathbf{e}_i \cdot \mathbf{n}, \tag{29}$$

where β is the anti-diffusion parameter and its value is taken as 0.7 [42]. After the color separation step, each particle distribution function undergoes streaming as given by Eq. (16). This multi-component model is only valid for fluids having similar density [36].

Further, we present a modeling framework to couple hydrodynamics with electrostatics in leaky dielectric fluids. When an electric field is applied to the multi-component fluid system, the transition of electrical properties leads to an electric stress (Maxwell stress) at the diffused interface. To account for the variation of electrical properties at the fluid–fluid interface, the local dielectric permittivity, ε, and electrical conductivity, σ, can be expressed as

$$\varepsilon(\mathbf{x},t) = \frac{\varepsilon_R \rho_R(\mathbf{x},t) + \varepsilon_B \rho_B(\mathbf{x},t)}{\rho_R(\mathbf{x},t)+\rho_B(\mathbf{x},t)}, \tag{30}$$

$$\sigma(\mathbf{x},t) = \frac{\sigma_R \rho_R(\mathbf{x},t) + \sigma_B \rho_B(\mathbf{x},t)}{\rho_R(\mathbf{x},t)+\rho_B(\mathbf{x},t)}, \tag{31}$$

where ε_R (ε_B) and σ_R (σ_B) are dielectric permittivity and electric conductivity of the red (blue) fluid, respectively. The electric stress is modeled by incorporating a body force due to electric field, $\mathbf{F}_E$, in the collision step. The body force $\mathbf{F}_E$ is given as [32]

$$\mathbf{F}_E = \nabla \cdot \underline{\mathbf{T}}^E = \rho_f \mathbf{E} - \frac{1}{2}E^2 \nabla \varepsilon. \tag{32}$$

This body force is incorporated through a source term using the formulation of Guo et al. [40] and is expressed as

$$\Phi_E = w_i \left(1 - \frac{1}{2\tau}\right)\left[\frac{\mathbf{e}_i - \mathbf{u}}{c_s^2} + \frac{(\mathbf{e}_i \cdot \mathbf{u})}{c_s^4}\mathbf{e}_i\right] \cdot \mathbf{F}_E. \tag{33}$$

where the corrected velocity $\mathbf{u}$ is now calculated as

$$\mathbf{u} = \frac{1}{\rho}\left[\sum_i f_i \mathbf{e}_i + \frac{1}{2}\left(\mathbf{F}_I + \mathbf{F}_E\right)\right]. \tag{34}$$

The inclusion of Φ_E with Φ_I results in the coupling of multi-component hydrodynamics with dynamics of leaky dielectric fluids.

2.3. Numerical method for leaky dielectric model

To incorporate Φ_E in the collision operation, it is first necessary to compute electric potential (U) in both the fluids. In electrostatics, Eq. (5) in terms of electric potential can be written as [34]

$$\nabla \cdot (\sigma \nabla U) = 0. \tag{35}$$

As the computational domain, shown in Fig. 1, is discretized on a uniform Cartesian grid, Eq. (35) can be solved by any suitable numerical method to obtain the distribution of U. In this study, the lattice Boltzmann equation proposed by He and Li [29] and finite-difference method (FDM) have been used separately to determine the quasi-steady distribution of electric potential (Eq. (35)). The computational efficiency of both the numerical methods is compared and discussed in Section 3.

In the framework of lattice Boltzmann method, an additional potential distribution function h_i can be defined that evolves according to

$$h_i(\mathbf{x}+\mathbf{e}_i\delta t, t+\delta t) - h_i(\mathbf{x},t) = -\frac{h_i(\mathbf{x},t) - h_i^{eq}(\mathbf{x},t)}{\tau_h}, \tag{36}$$

where

$$h_i^{eq}(\mathbf{x},t) = w_i U(\mathbf{x},t), \quad i = 0, 1, 2 \ldots N. \tag{37}$$

Here, h_i^{eq} is the local equilibrium potential distribution function, U is the macroscopic electric potential, w_i is the weight function and $\mathbf{e}_i$ is the microscopic velocity. In Eq. (36), τ_h is the dimensionless electric relaxation time defined as

$$\tau_h = 3\sigma(\mathbf{x},t) + 0.5. \tag{38}$$

The velocity vectors and the weight functions for the individual directions are the same as given in Eqs. (10)–(13).

The macroscopic electric potential U can be obtained by zeroth-order moment of h_i as

$$U(\mathbf{x},t) = \sum_i h_i(\mathbf{x},t). \tag{39}$$

As shown in Appendix A, on applying the Chapman–Enskog expansion, Eq. (36) can be shown to reduce to

$$\frac{\partial U}{\partial t} - \nabla \cdot (\sigma \nabla U) = 0. \tag{40}$$

Eq. (40) is equivalent to Eq. (35) under the steady state limit (i.e. $\partial U/\partial t = 0$). Thus, in this work we have evaluated this method of solving Eq. (35) using an additional distribution function h_i.

When using the finite-differencing scheme, the gradients of electrical conductivity and electric potential in Eq. (35) are approximated by using the second-order central differencing scheme at the interior nodes and second-order forward or backward differencing scheme at the boundary nodes of the computational domain. The obtained discretized equation is then solved by using point Gauss–Seidel or alternate direction implicit (ADI) scheme to compute the quasi-steady distribution of electric potential at each time instant.

2.4. Algorithm

The steps involved in the implementation of the algorithm developed for coupling the multi-component lattice Boltzmann method and the leaky dielectric model is described in the flow chart shown in Fig. 2. The D2Q9/D3Q19 model of lattice Boltzmann method, as shown in Fig. 1, is adopted to perform simulations. Firstly, the initial and boundary conditions of density, velocity and electric potential are specified. Next, using an iterative procedure a time invariant quasi-steady distribution of electric potential is computed at each time instant. The electric potential U is considered to have reached a steady-state when

$$\frac{\left|U^n - U^{n-1}\right|}{|U^n|} < \delta_U, \tag{41}$$

where $\delta_U = 10^{-6}$ is the tolerance and n represents the nth iteration. Subsequently, ρ_f and electric field distribution ($E = -\nabla U$) [34] in the computational domain are determined. Finally, the source term due to electric field Φ_E is computed at each lattice and is incorporated in collision step of the velocity distribution function. These steps are repeated to simulate EHD of leaky dielectric fluids at each time instant.

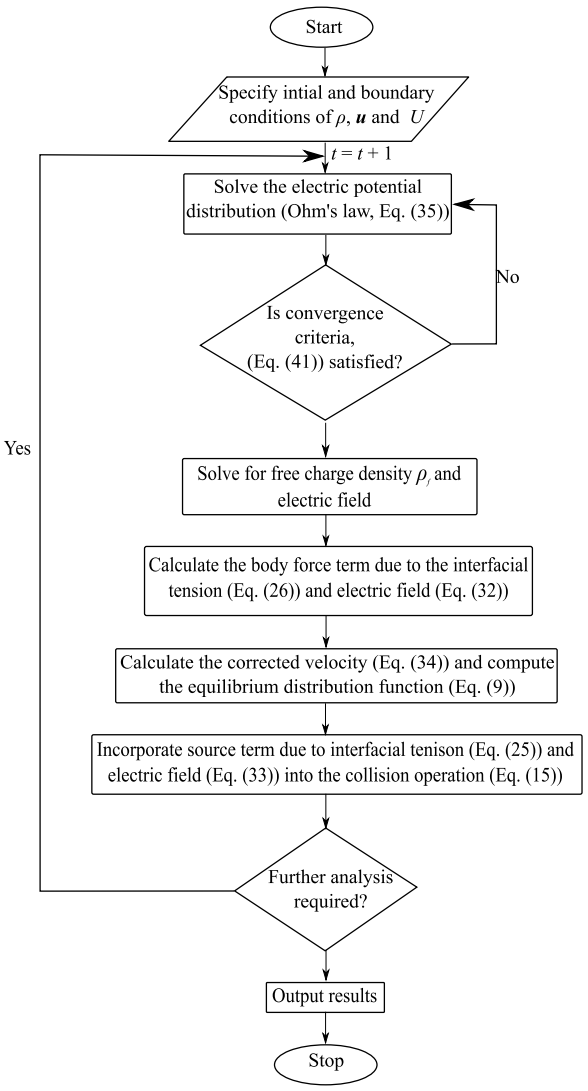

Fig. 2. Flow chart for coupling lattice Boltzmann method and leaky dielectric model.

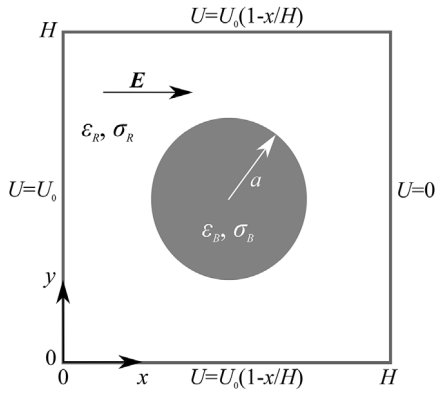

Fig. 3. Illustration of the computational domain for comparing the computational efficiency of the numerical methods for solving Eq. (35). A droplet is suspended in another immiscible fluid at the center of the computational domain. Electric field is acting along the horizontal direction. A linearly varying electric potential is applied along the top and the bottom boundaries. The subscripts B and R denote the inner and the outer fluids, respectively.

Table 1
LBM values corresponding to the physical parameters used to obtain a steady solution.

Parameter	LBM values
Density of red fluid	1.0
Density of blue fluid	1.0
Kinematic viscosity of red fluid	1.0
Kinematic viscosity of blue fluid	1.0
Interfacial tension	0.01
Electrical conductivity of red fluid	0.10
Electrical conductivity of blue fluid	0.20
Dielectric permittivity of red fluid	0.01
Dielectric permittivity of blue fluid	0.005

Table 2
Comparative analysis of the number of iterations and computation time taken by the numerical techniques to compute Eq. (35). The number of iterations have been rounded off to two significant digits.

Numerical method	Lattice Boltzmann method	Point Gauss–Seidel	ADI
Iterations	280 000	83 000	27 000
Computation time (s)	9962.31	400.80	335.72

3. Results and discussion

Firstly, a comparative analysis was carried out to calculate the number of iterations required for computing a time invariant electric potential using the lattice Boltzmann method [29], point Gauss–Seidel method and alternate direction implicit (ADI) method. As a model problem, a droplet suspended in another immiscible fluid was considered with an electric field acting on both the fluids along the horizontal direction. A schematic of the computational domain is shown in Fig. 3. The size of the computational domain is taken as $20a \times 20a$, where $a = 20\Delta x$ is the droplet radius. The left boundary of the domain is considered at higher potential and the right boundary is grounded. A linearly varying electric potential is applied along the top and the bottom boundaries of the domain. The subscripts B and R denote the inner and the outer fluids, respectively. The conductivity and permittivity ratios were taken as $\sigma_B/\sigma_R = 2$ and $\varepsilon_B/\varepsilon_R = 0.5$, respectively. The LBM parameters in Table 1 were determined by using the scaling factors mentioned in Table B.1 (Appendix B).

Table 2 shows the comparison of the number of iterations taken by the lattice Boltzmann method, point Gauss–Seidel and the alternate direction implicit (ADI) method to obtain a time invariant electric potential distribution in the domain. The slow rate of convergence of the lattice Boltzmann method to attain a steady solution is in consistence with the observations of Patil et al. [43]. Because it required the least number of iterations and computation time, the ADI scheme was used to compute the distribution of the electric potential in the case studies presented hereafter. Further improvements in achieving faster convergence are possible by using numerical schemes such as conjugate gradient, multi-grid method etc.

Next, three different scenarios have been analyzed to validate our model. In the first case study, simulations were performed for a droplet suspended in another immiscible fluid in the presence of an electric field. The flow patterns induced in the droplet were qualitatively validated with previous numerical and experimental studies. Further, the deformations obtained by individually varying the electric field and the interfacial tension were compared with analytical results. In the second case study, the flow dynamics of a pair of circular droplets initially separated from each other in the presence of an electric field was compared with earlier studies. Lastly, the dynamics of a droplet under the combined effect of electric field and shear flow was analyzed. In all the case studies, the droplet radius was taken as $20\Delta x$. The parameters used for carrying out simulations were selected in a manner that the

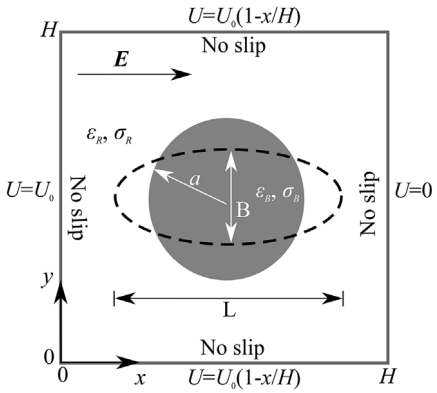

Fig. 4. Schematic of the computational domain for simulating the effect of electric field on a droplet. The droplet is suspended in another immiscible fluid at the center of the computational domain. The density of the droplet and the outer fluid is considered to be equal. No slip hydrodynamic boundary condition is applied along the domain boundaries. The left boundary of the domain is at higher potential and the right boundary is grounded. A linearly varying potential is applied along the top and the bottom walls of the domain. The subscripts B and R denote the inner and the outer fluids, respectively.

charge relaxation time was significantly smaller than the viscous relaxation time, i.e., $t_c \ll t_v$ where $t_c = \varepsilon_R/\sigma_R$ and $t_v = \mu_R/\varepsilon_R E^2$.

3.1. Droplet deformation

In the first scenario simulated, the deformation induced in a droplet in the presence of an electric field is presented and the results are compared with an analytical solution [15]. Fig. 4 illustrates the schematic of the problem solved. A droplet of initial radius a is immersed in another immiscible fluid and an electric field **E** is acting on the fluids along the horizontal direction. Under the influence of electric field, the charge accumulates at the drop interface and induces an electric stress along both the normal and tangential directions to the fluid–fluid interface. Depending upon the distribution of this free charge, the tangential stress induces recirculatory fluid flow thereby generating hydrodynamic stress at the drop interface. This interaction between the electric and hydrodynamic stress leads to the deformation of the droplet into either a prolate (along the direction of electric field) or an oblate (normal to the direction of electric field) shape [8].

The deformation, D, induced in the droplet can be quantified as

$$D = \frac{L - B}{L + B}, \tag{42}$$

where L and B are the end-to-end lengths of the droplet measured along and in a direction transverse to the electric field as shown in Fig. 4, respectively. In Stokes flow limit, the droplet deformation at steady-state can be expressed as

$$D = \frac{d\varepsilon_B E^2 a}{3S(1+R)^2\gamma}, \tag{43}$$

where

$$d = R^2 + R + 1 - 3S. \tag{44}$$

Here, γ is the interfacial tension, $R = \sigma_B/\sigma_R$ is the conductivity ratio and $S = \varepsilon_B/\varepsilon_R$ is the permittivity ratio. It should be noted that Eq. (43) is only applicable for $D \ll 1$ [15]. In Eq. (43), d is a discriminating function which dictates the deformation shape of the droplet. For $d > 0$, the droplet deforms into a prolate shape while an oblate shape is obtained for $d < 0$. Moreover, the direction of flow field induced in the two fluids is determined from the relative magnitude of R and S [6,8,15]. For $R < S$ the velocity vectors in the first quadrant are oriented in the anti-clockwise direction (from the poles to the equator), whereas for $R > S$ the velocity vectors are along the clockwise direction (from the equator to the poles).

Table 3
Droplet radius and grid spacing used in grid independence study.

Description	Droplet radius	Grid resolution
Mesh 1 (coarse grid)	$10\Delta x$	200×200
Mesh 2 (regular grid)	$20\Delta x$	400×400
Mesh 3 (fine grid)	$30\Delta x$	600×600

A computational domain of size $20a \times 20a$ was considered to simulate the dynamics of the droplet under the influence of electric field. To apply an electric field, the left boundary of the domain was considered at higher potential and the right boundary was grounded. A linearly varying electric potential was applied along the top and the bottom boundaries of the domain. No slip hydrodynamic boundary condition was imposed on all the domain boundaries by implementing the half-way bounce back scheme. The density of the inner and the outer fluids was considered to be equal. Flow parameters were selected to ensure that $Re = 0.1$ so as to compare simulation results with the analytical solution (Eq. (43)) [15].

The results obtained for the droplet deformation and the fluid motion for three different cases (i) $R > S$, $d > 0$, (ii) $R < S$, $d > 0$ and (iii) $R < S$, $d < 0$ are shown in Fig. 5(a)–(c), respectively. Fig. 5(a) shows that the velocity vectors in the first quadrant are in the clockwise direction and the droplet deforms into a prolate shape. Fig. 5(b) and (c) show that the velocity vectors in the first quadrant are along the anti-clockwise direction and the droplet deforms into a prolate and an oblate shape, respectively. The flow patterns obtained from our simulations are in agreement with earlier analytical and experimental studies [8,44,45].

Simulations were also carried out to quantify the deformations induced in the droplet by varying (a) the electric field and (b) the interfacial tension. To ensure the mesh independence of numerical results, a grid sensitivity study was performed by comparing the results obtained with three different mesh sizes. The description of the grid spacing and droplet radius is given in Table 3. A comparison of the deformations induced in the droplet under the influence of electric field for all the mesh resolutions is shown in Fig. 6. The electric field E has been normalized by the maximum value of electric field $E_0 = U_{max}/H$. Here U_{max} is the maximum electric potential applied and H is the distance between the two electrodes for each grid. As the results obtained using the mesh of 400×400 show good agreement with the fine grid, hence it was adopted for conducting further simulations.

Fig. 7(a) and (b) show a comparison of the droplet deformation D obtained from our formulated model and the analytical solution (Eq. (43)) for different values of electric field and interfacial tension, respectively. The solid lines in Fig. 7 denote the theoretical deformations whereas the symbols denote the results from the model formulated in this work. The deformations induced in the droplet calculated from our model are in agreement with the analytical results [46]. As the analytical expression [46] is applicable only for small deformations ($D \ll 1$), the results predicted from the analytical solution deviate slightly from those obtained from our model as D approaches 0.1.

Further, simulations were performed to validate the time evolution of deformation induced in the droplet due to an electric field. The gradual evolution of the droplet deformation with time was examined in a confined geometry and the results obtained were compared with the work of Santra et al. [47]. The confinement ratio $\chi = 2a/H$ was considered as 0.2 and the electrical conductivity

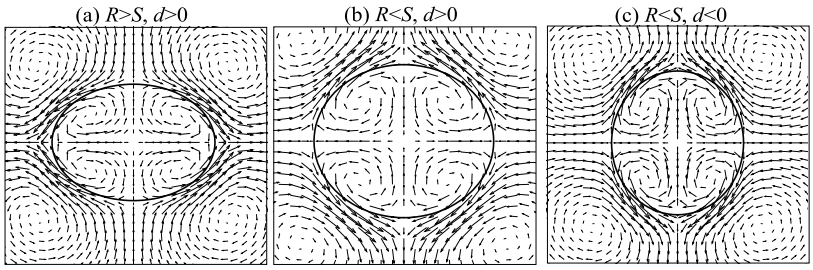

Fig. 5. Droplet deformation and circulatory flow induced in the fluid domain in the presence of an electric field. (a) For $R > S, d > 0$, droplet deforms into a prolate shape and velocity vectors in the first quadrant move along the clockwise direction. (b) Droplet deforms into a prolate shape for $R < S, d > 0$ and velocity vectors in the first quadrant move along the anti-clockwise direction. (c) For $R < S, d < 0$, flow field in the first quadrant is induced along the anti-clockwise direction and the droplet deforms into an oblate shape.

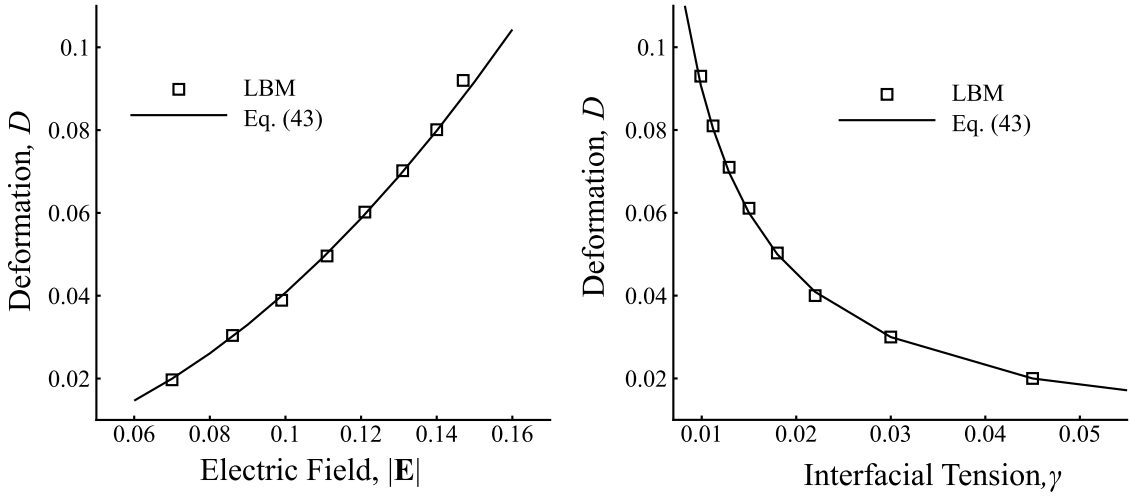

Fig. 7. Comparative analysis of the droplet deformation D between the analytical solution and the model formulated in the present work by altering (a) electric field, $|\mathbf{E}|$ and (b) interfacial tension, γ. The solid line in the figure represents the analytical results and symbols denote the work from our developed model.

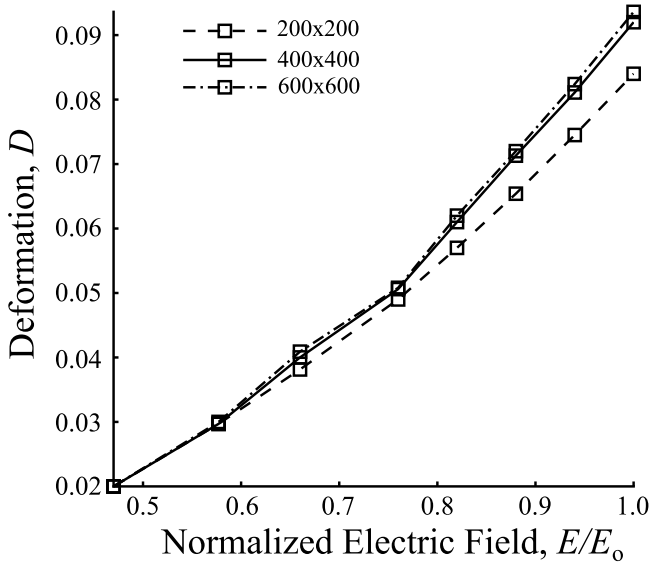

Fig. 6. Comparative analysis of the deformations induced in the droplet under the influence of electric field for different mesh resolutions. The electric field has been normalized by the maximum value of electric field $E_o = U_{max}/H$ occurring in the respective mesh resolutions. The description of the mesh resolution is shown in Table 3.

and permittivity ratio were taken as 2 and 0.5, respectively. The size of the computational domain was taken as $10a \times 20a$. The time evolution of the droplet deformation were analyzed for two different electric capillary number $Ca_E = \varepsilon_R E^2 a/\gamma = 0.08$ and 0.14 at $Re = 0.01$, respectively. Fig. 8 shows a comparison of the evolution of the droplet deformation obtained from our model with the numerical results of Santra et al. [47]. The solid lines in Fig. 8 denote the results from our multi-component and the symbols represent the results of Santra et al. Clearly, the results obtained from our multi-component model are in good agreement with the results of [47].

3.2. Droplet pair interaction

In the second case study, the behavior of a pair of circular droplets suspended in another immiscible fluid under the influence of an electric field was analyzed. This problem has been previously analyzed by Baygents et al. [6] for spherical droplets using the boundary integral method in the Stokes flow limit and a qualitative comparison is presented with our two-dimensional simulations. As shown in Fig. 9, a pair of droplets each with an initial radius a were separated by a center-to-center distance of $h = 5.0a$. A uniform electric field $\mathbf{E}$, far from the droplets, was acting parallel to the line passing through the droplet centers. It was reported that the dynamics of the droplet pair, initially separated at sufficiently large distance from each other, is affected by two different mechanisms acting simultaneously on them. First, in the presence of an electric field, free charge accumulates on the fluid interface and the droplets behave like a dipole. This electric interaction between the droplet pair is always attractive in nature and leads to the coalescence of droplets. Secondly, the flow induced pushes the droplets either towards or away from each other depending

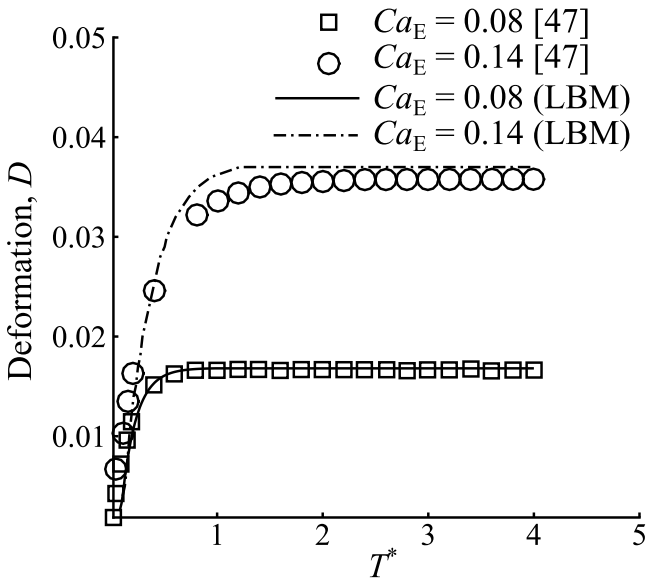

Fig. 8. Comparison of the evolution of droplet deformation in a confined geometry due to an electric field. The confinement ratio is taken as $\chi = 0.2$, the conductivity and permittivity ratios are taken as 2 and 0.5, respectively. Here $T^* = t/t_v$ is the non-dimensional time. The symbols indicate the results of Santra et al. [47] and the lines represent the results obtained from our developed model.

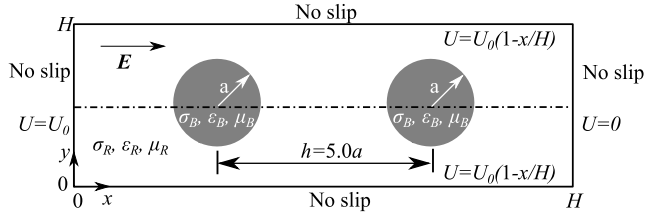

Fig. 9. Schematic of the computational domain for simulating the effect of an electric field on a pair of droplets. The droplets are separated by a center-to-center distance of 5 times the droplet radius. The density and viscosity of both the droplets and the outer fluid are considered same. No slip boundary condition is applied at the domain boundaries. The left boundary of the domain is considered to be at higher potential and the right boundary is grounded. A linearly varying electric potential is applied at the top and the bottom walls of the domain. The subscripts B and R denote the droplets and the outer fluid, respectively.

upon the orientation of recirculations produced. Baygents et al. [6] inferred that although the electrostatic interactions always act on the droplets, the effective motion of the droplet pair is governed by the direction of flow field induced, which further depends upon the sign of $(R - S)$, where $R = \sigma_B/\sigma_R$ is the conductivity ratio and $S = \varepsilon_B/\varepsilon_R$ is the permittivity ratio. The droplet pair was reported to move towards each other for $R < S$ whereas, the droplet pair moves away from each other for $R > S$.

To capture the attractive and the repulsive nature of this interaction, we performed simulations for both conditions corresponding to $R < S$ and $R > S$. The domain size was taken as $35a \times 35a$ (where a is the droplet radius) and was chosen in a manner such that the electric field far from the droplets becomes uniform. To impose an electric field, the left boundary of the domain was considered at higher potential and the right boundary was grounded. A linearly varying electric potential was imposed along the top and the bottom boundaries of the domain. Also, no slip hydrodynamic boundary condition was enforced along all the domain boundaries by implementing half-way bounce back scheme. The flow parameters used for carrying out simulations were selected such that $Ca_E = \varepsilon_R E^2 a/\gamma = 1.5$ and the fluid flow lies in Stokes flow limit ($Re \ll 1$).

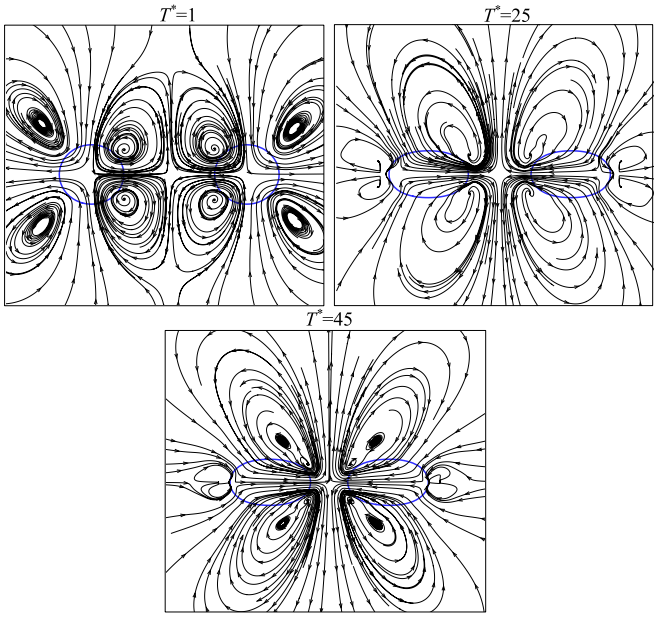

Fig. 10. Droplet pair interaction and the streamline patterns induced at different time $T^* = t/t_v$ for $R = 6$ and $S = 8$ at $Ca_E = 1.5$.

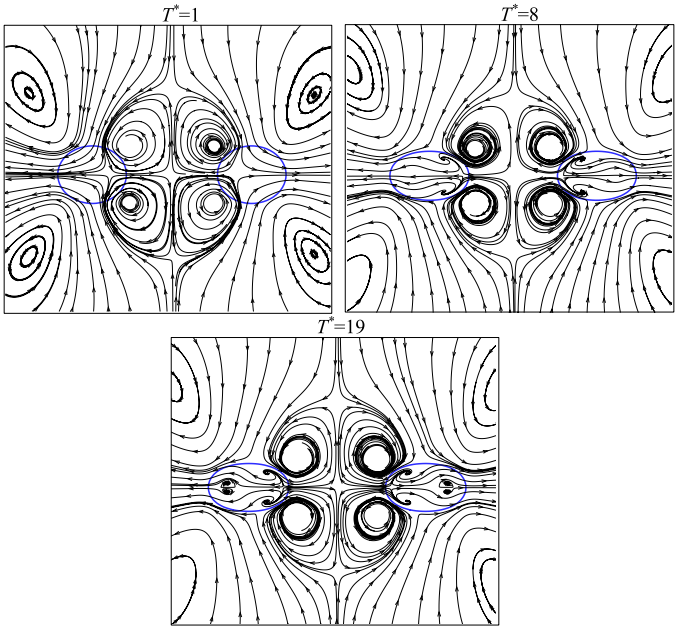

Fig. 11. Droplet pair interaction and the streamline patterns induced at different non-dimensional time $T^* = t/t_v$ for $R = 1.04$ and $S = 0.2$ at $Ca_E = 1.5$.

The results of droplet pair interaction for $R < S$ and $R > S$ obtained from our simulations are shown in Figs. 10 and 11, respectively. The deformed droplet shape and the direction of streamlines induced in the domain are shown for different time instants using a non-dimensional time, $T^* = t/t_v$. For $R < S$, the droplets deform along the direction of electric field and the flow inside the droplets moves from equator to poles. Such evolution of flow pattern clearly suggests that the droplets exhibit movement towards each other. For $R > S$, although the droplets stretch along the direction of electric field, the flow evolves from poles to equator with time. These flow patterns result in increasing the separation between the two droplets and confirms the earlier observations where similar behavior for $R > S$ has been reported [6]. Even though our

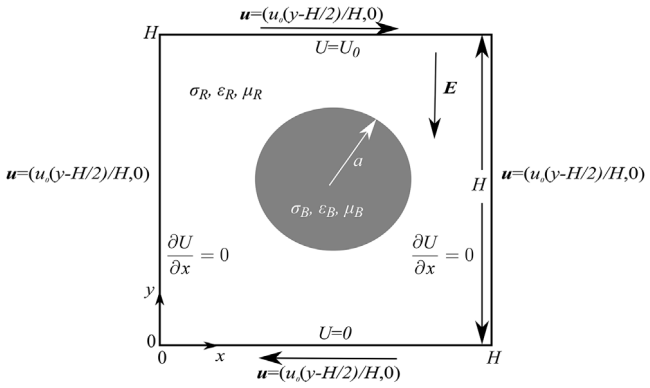

Fig. 12. Schematic of the computational domain for simulating the cumulative effect of electric field and shear force on droplet deformation. The density and viscosity of the droplet and the outer fluid are considered to be equal. The top and bottom boundaries of the domain move with velocity $u = u_0(y-H/2)/H$. A constant electric potential is applied at the top boundary of the domain and the bottom boundary is grounded. The left and right boundaries of the domain are electrically insulated. The subscripts B and R denote the inner and the outer fluids, respectively.

simulations are two-dimensional, the results are consistent with the results of Baygents et al. [6].

3.3. Droplet behavior in a shear flow and electric field

The applicability of the developed numerical model is further highlighted by simulating the effect of electric field and externally imposed shear stress acting simultaneously on a droplet. This model problem was previously solved by using the immersed boundary and immersed interface method (IBIIM) at Ohnesorge number $Oh = \mu/\sqrt{(\rho\gamma a)} = 1$ and electric capillary number $Ca_E = \varepsilon_R E^2 a/\gamma = 1$ [22]. We present validation of our model by comparing the deformed droplet shapes obtained from our simulations with the results of Ref. [22].

A schematic of the computational domain is shown in Fig. 12 with a droplet suspended in another immiscible fluid. The outer fluid is subjected to a shear flow by applying a velocity $\mathbf{u} = (u_0(y - H/2)/H, 0)$ at the top and the bottom plates, respectively. The top boundary of the domain is considered at higher potential, the bottom boundary is grounded and the vertical boundaries are electrically insulated (i.e. $\partial U/\partial x = 0$). The ratio of the droplet radius to the domain size $2a/H$ is 1/8. The hydrodynamic boundary conditions were implemented by applying periodic boundary conditions along the left and right boundaries of the domain. For the moving boundaries, half-way bounce back scheme given as

$$f_{i,k}(\mathbf{x}, t + \delta t) = f_{i',k}(\mathbf{x}, t) + 2\frac{\rho_k w_i}{c_s^2}\mathbf{u} \cdot e_i, \tag{45}$$

was implemented on the top and bottom boundaries of the domain. Here i' is the direction opposite to i and k refers to the "red" or "blue" fluid. The flow parameters used for carrying out the simulations were selected such that $Oh = 1$, $Ca_E = 1$ and $\mathrm{Re} = O(1)$.

The presence of the inner fluid droplet disturbs the motion of the outer fluid. This disturbance induces stress both along the tangential and the normal direction at the drop interface. The normal stress leads to a pressure difference across the interface thereby deforming the droplet. As stated in Section 3.1, applying an electric field on fluids induces an electric stress at the fluid–fluid interface. Thus, the deformation of droplet under the combined effect of electric field and shear flow is governed by the cumulative effect of electric and shear stresses acting at the drop interface.

Fig. 13 shows the comparison of the droplet deformation due to shear flow with (solid line) and without (dotted line) an applied electric field at a non-dimensional time $T^* = t/(\rho a^3/\gamma)^{1/2} = 10$. The parameters used for comparison were (i) $R = 1.75$, $S = 3.5$, (ii) $R = 3.25$, $S = 3.5$ and (iii) $R = 4.75$, $S = 3.5$ as shown in Fig. 13(a)–(c), respectively. Here, $R = \sigma_B/\sigma_R$ is the conductivity ratio and $S = \varepsilon_B/\varepsilon_R$ is the permittivity ratio. As illustrated by the dotted lines, the droplet elongates due to shear flow into an ellipsoidal shape and inclines at an angle to the horizontal flow direction. As stated in Section 3.1, the deformation of a droplet in the presence of an electric field can be determined by discriminating function, d. The value of $R = 1.75$ and $S = 3.5$ results in $d < 0$ (Eq. (44)), thus under the combined effect of electric field and shear flow the droplet tends to align itself towards the horizontal direction. Similarly, in Fig. 13(b) and (c), the value of R and S results in $d > 0$ (Eq. (44)) thereby leading to a higher angular separation between the droplet major axis and the shear direction. Fig. 14(a)–(c) show the comparison of these results, corresponding to the three cases shown in Fig. 13 at $Ca_E = 1$, obtained from our simulations with the results of Hu et al. [22]. The solid lines represent the results obtained from the present method and the symbols denote the results from immersed boundary and immersed interface method [22]. Clearly, the results obtained from our simulations are in very good agreement with published results.

Furthermore, the streamline patterns corresponding to the results of Fig. 14 were analyzed and are shown in Fig. 15. For $R = 1.75$ and $S = 3.5$, the drop interface is tangential to the local streamlines and separates the recirculation zone inside the droplet from the outer fluid. Also, the streamline patterns do not cross the interface thereby indicating that a steady deformed shape has been reached [48]. Similarly, streamline patterns for $R = 3.25$ and $S = 3.5$ also indicate that an equilibrium shape has been attained. For $R = 4.75$ and $S = 3.5$, it can be seen from Fig. 15(c) that streamlines pass through the fluid interface, suggesting that the equilibrium shape has not been attained at $T^* = 10$ and a longer computation time is needed for the droplet to reach a steady state. These results are also in qualitative agreement with Mählmann and Papageorgiou [48].

The results from the above case study highlight the effect of an externally applied electric field on a droplet placed in a Couette flow configuration. Since the behavior of a single isolated spherical droplet can provide a fundamental understanding in the synthesis of emulsion in micro-confined flows, the developed method has been applied to examine the effect of an electric field on a spherical droplet placed in a confined ($H/2a < 4$) Couette flow configuration. A schematic of the computational domain depicting a spherical droplet of radius a suspended in another immiscible fluid is shown in Fig. 16. The top and bottom walls of the domain are separated from each other by a distance $H = 4.0a$ and translate along the x-direction with velocity $\mathbf{u} = (u, 0, 0)$ and $\mathbf{u} = (-u, 0, 0)$, respectively. The top and bottom walls of the domain as prescribed fixed with unequal electric potential.

The top wall of the domain is considered at higher potential and the bottom wall is grounded. The hydrodynamic boundary conditions were implemented by applying half-way bounce back scheme for the top and bottom walls of the domain, as given by Eq. (45). Periodic boundary conditions were applied along the flow and traverse boundaries of the domain.

As stated above, the presence of a droplet in Couette flow configuration induces stress both along the normal and the tangential direction to the droplet interface. This leads to the deformation of the droplet into an ellipsoidal shape with its major axis inclined at an angle with the flow direction or sometimes even breakup of the droplet into smaller droplets. For a fixed viscosity ratio $\lambda = \mu_B/\mu_R$ and confinement ratio $\chi = 2a/H$ the droplet behavior in the Stokes flow limit can be characterized by the Capillary number, $Ca = \zeta a \mu_R/(\gamma)$, where $\zeta = 2u/H$. For $Ca < Ca_{crit}$ (critical Capillary number), the droplet deforms and attains a steady shape while for $Ca \geq Ca_{crit}$ the droplet breaks up into smaller droplets [49–51].

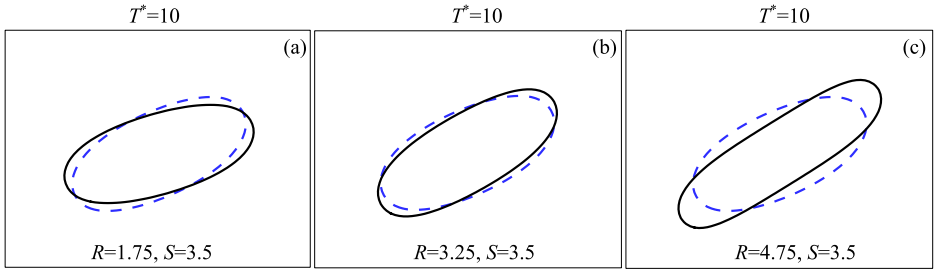

Fig. 13. Comparison of the deformations induced in a droplet due to shear flow with (solid line) and without (dashed line) electric field at a non-dimensional time $T^* = t/(\rho a^3/\gamma)^{1/2} = 10$. (a) The angular separation between the major axis of the droplet and the direction of shear flow decreases in the presence of electric field as compared to without electric field. (b) and (c) depict that the angular separation between the major axis of the droplet and the direction of shear flow increases in the presence of electric field than in the absence of electric field.

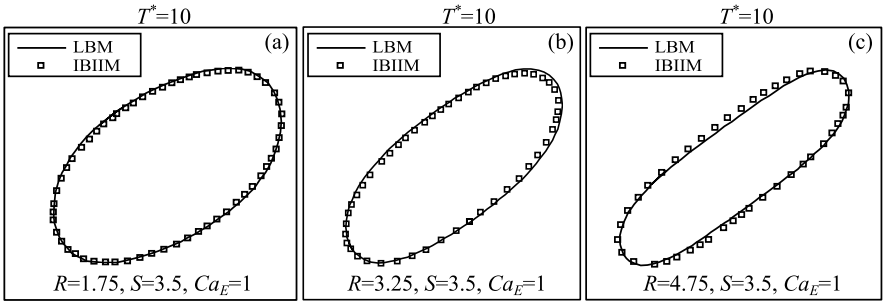

Fig. 14. Comparison of the droplet shape obtained from the model formulated in the present work and immersed boundary and immersed interface method. The solid lines represent the work from the present study and the symbols denote the results of Hu et al. [22].

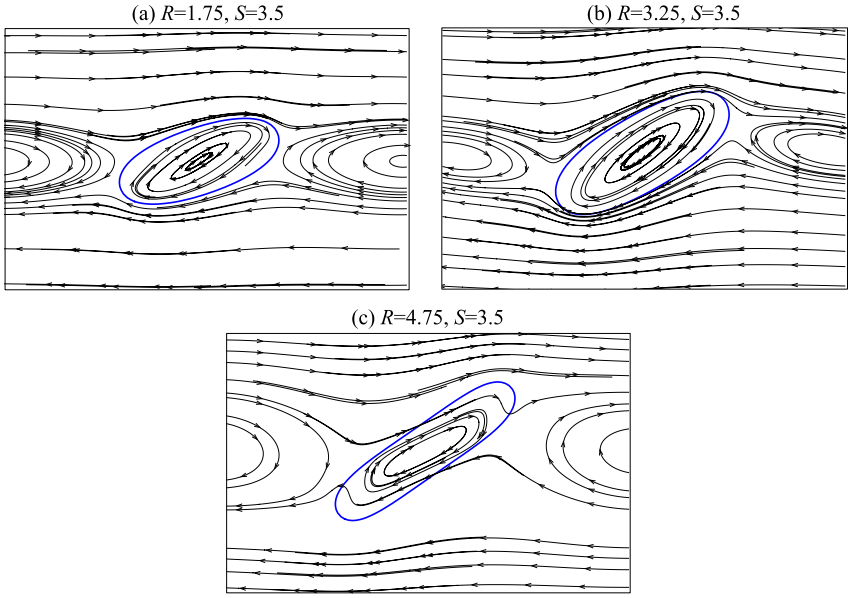

Fig. 15. Streamline patterns of the drop suspended in shear flow at $Oh = 1$ and $Ca_E = 1$.

The cumulative effect of the electric and viscous stresses were analyzed by examining the dynamics of the droplet for $Ca = 0.4$ at $Ca_E = 0$ and $Ca_E = 0.2$. The droplet and the surrounding fluids were considered to be of equal viscosity. The size of the computational domain was taken as $16a \times 4a \times 4a$. The electric conductivity and dielectric permittivity ratio of the fluids were taken as $R = 10$ and $S = 2$, respectively. Fig. 17 shows the variation in droplet profile with time for $Ca = 0.4$ and $Ca_E = 0$. The viscous shear stresses of the external flow leads to the elongation of the droplet ($\zeta t = 5$ and 15). At $\zeta t = 20$, a waist is formed at the center of the droplet and the further elongation of the droplet results in the formation of two bulbous ends connected from each other by a neck ($\zeta t = 26$). The neck continues to thin ($\zeta t = 29$), eventually leading to the binary breakup of the droplet ($\zeta t = 30$ and $\zeta t = 33$). The continuous elongation of the droplet eventually leading to the binary breakup of the droplet is in agreement with the work of Janssen et al. [50] and also validates quantitatively with the work of Liu et al. [52].

Applying an electric field to the droplet leads to a significant increase in the deformation of the droplet. The evolution of the droplet profile with time is shown in Fig. 18. The interplay of the electric and viscous stresses results in a sigmoidal shape of the droplet with the droplet ends pointing towards the electrode ($\zeta t = 5$ and 7). Further elongation of the droplet leads to the

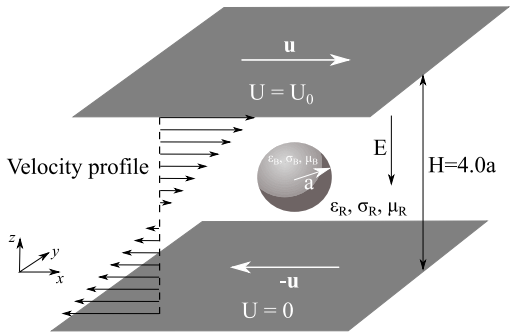

Fig. 16. Illustration of the computational domain for simulating the droplet breakup in a confined Couette flow configuration under the influence of an electric field. A droplet of radius a is placed in the center of the computational domain. The top and bottom walls are separated from each other by a distance $H = 4.0a$. The density and viscosity of both the droplet and the outer fluid are considered same. Moving wall hydrodynamic boundary condition is applied along the top and bottom walls of domain. Periodic boundary condition is applied along the flow and traverse direction of the domain. The top wall is considered to be at the higher potential and the bottom wall is grounded. The subscripts B and R denote the droplet and the outer fluid, respectively.

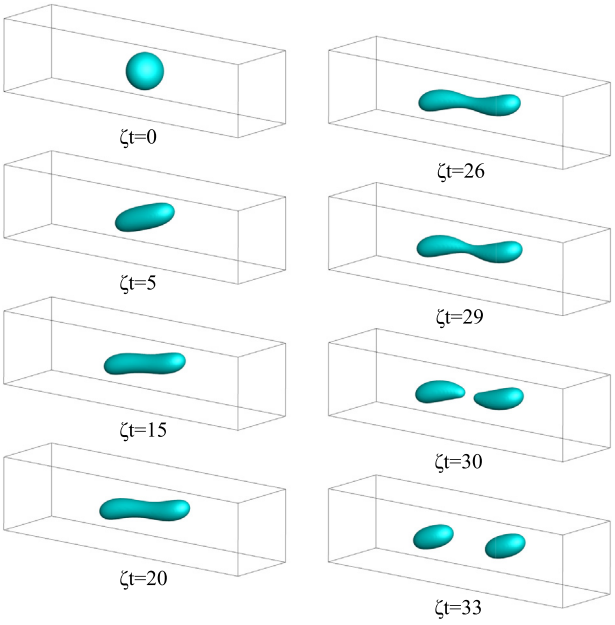

Fig. 17. Shape evolution of the droplet in a confined Couette flow configuration for $Ca = 0.4$, $Ca_E = 0$ and $\lambda = 1$. The conductivity and permittivity ratio of the fluids are $R = 10$ and $S = 2$, respectively.

formation of rounded ends ($\zeta t = 15$). The center portion of the droplet continues to thin, eventually leading to the development of pinching region near the droplet ends ($\zeta t = 20$). Subsequently, the bulbous ends split ($\zeta t = 22$) and the remaining droplet retracts under the action of interfacial force to from an ellipsoidal droplet in the center ($\zeta t = 26$). As compared to $Ca_E = 0$, for $Ca_E = 0.2$ the droplet deformation increases significantly and the droplet breaks up into three smaller droplets (ternary break up). Thus, for a set of flow parameters, it can be inferred that the inclusion of an electric field can promote the breakup of a droplet in confined flow system. Further detailed analysis of the droplet dynamics in a confined flow and under the influence of an electric field will be presented in a future work.

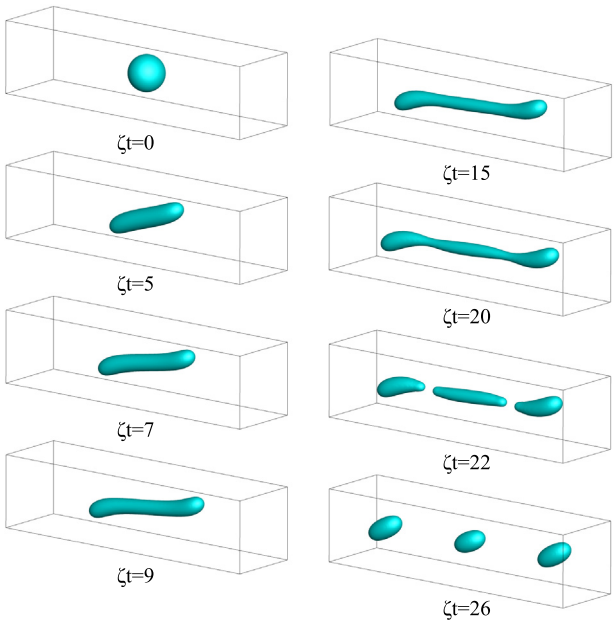

Fig. 18. Shape evolution of the droplet in a confined Couette flow configuration for $Ca = 0.4$, $Ca_E = 0.2$ and $\lambda = 1$. The conductivity and permittivity ratio of the fluids are $R = 10$ and $S = 2$, respectively.

The validation of the above case studies show that the developed approach of coupling the low spurious current multicomponent model of the lattice Boltzmann method with the leaky dielectric model can accurately predict the physics of leaky dielectric fluids under the influence of an electric field. Although models have been attempted to simulate the electrohydrodynamics of multicomponent fluids in the framework of the lattice Boltzmann method, the key differences between our work and these earlier studies has been in the choice of the hydrodynamics model (low vs. high spurious velocity at the interface) [27,30] and computational efficiency of the methodology to simulate the flow physics of leaky dielectric fluids. Further, the formulated methodology is applicable for both steady and time evolving electrohydrodynamic flows and can be used in modeling a variety of electric field actuated multiphase flows such as droplet manipulation in an electrified microchannel [53,54], production of droplets under the influence of an electric field in a microchannel [55,56] and droplet sorting using dielectrophoresis in a microfluidic system [57].

4. Conclusions

In this work, the capability of lattice Boltzmann model in simulating flows involving interfacial dynamics has been utilized to compute electrohydrodynamic flows in leaky dielectric fluids. The developed framework involves coupling of the leaky dielectric model with a low spurious current multi-component lattice Boltzmann model by calculation of the Maxwell stresses and their inclusion in the hydrodynamics equation. The developed model involves computation of a time invariant steady electric potential distribution in the flow domain using a time marching lattice Boltzmann equation or through a finite-difference formulation. As compared to point Gauss–Seidel and alternate direction implicit methods, the rate of convergence of the lattice Boltzmann equation to attain a steady electric potential distribution was observed to be slow. Using alternate direction implicit scheme, the steady electric potential distribution was computed for steady and time evolving electrohydrodynamic flows. The developed model was validated with three different case studies. In the first flow scenario

modeled, simulations were carried out to compute the steady state deformation of a droplet suspended in another immiscible fluid under the action of an external electric field. Under the small deformation limit, the deformation induced in the droplet by varying the electric field and interfacial tension were in excellent agreement with analytical results. Further, the flow fields induced in the flow domain were also in good agreement with the previous analytical and experimental results. In the second case study, the interaction of a pair of circular droplets suspended in another immiscible fluid in the presence of an external electric field was analyzed. It was shown that the droplet pair either moved towards or away from each other due to competing effect of induced flow and electrostatic interaction (attractive or repulsive) at the section of interface closest to each other. The elongation induced in the droplet pair and the evolution of flow patterns in the flow domain were in qualitative agreement with an earlier study. Lastly, the combined effect of external electric field and shear flow on a droplet suspended in an outer fluid was simulated. The time evolution of the droplet shape with and without electric field for a fixed permittivity ratio and various conductivity ratios was analyzed. The results obtained were in congruence with the previously reported numerical studies. The developed methodology was further extended to three-dimensional flows to examine the behavior of a spherical droplet under the influence of an electric field in confined flows. The evolution of the droplet profile with time both in the presence and absence of the electric field was examined. The inclusion of electric field in the confined flow configuration was observed to increase the deformation of the droplet and promotes the breakup of the droplet into smaller droplets. It is expected that the developed model will be of benefit in modeling a variety of electric field actuated multiphase flows in the near future.

Acknowledgment

This research did not receive any specific grant from funding agencies in the public, commercial, or not-for-profit sectors.

Appendix A

The derivation of the Ohm's law from the lattice Boltzmann equation proposed by He and Li [29] is as follows. Considering a generalized case, *DdQq* model, where d, q are number of dimensions and possible velocities, respectively, the evolution equation of electric potential distribution function (h_i) is

$$h_i(\mathbf{x}+\mathbf{e}_i\delta t, t+\delta t) - h_i(\mathbf{x}, t) = \frac{-1}{\tau_h}(h_i(\mathbf{x}, t) - h_i^{eq}(\mathbf{x}, t)), \tag{A.1}$$

where τ_h is the electric relaxation time and h_i^{eq} is the local equilibrium electric potential distribution function. On expanding $h_i(\mathbf{x}+\mathbf{e}_i\delta t)$ using Taylor series expansion the evolution equation can be written as

$$D_i h_i(\mathbf{x}, t) + \frac{\delta t}{2!}D_i^2 h_i(\mathbf{x}, t) = -\frac{1}{\tau_h \delta t}(h_i(\mathbf{x}, t) - h_i^{eq}(\mathbf{x}, t)), \tag{A.2}$$

where

$$D_i = \frac{\partial}{\partial t} + \mathbf{e}_i \cdot \nabla. \tag{A.3}$$

By using the Chapman–Enskog [58] approximation in time and space, we have

$$\frac{\partial}{\partial t} = \epsilon^2 \frac{\partial}{\partial t_2}, \tag{A.4}$$

$$h_i(\mathbf{x}, t) = h_i^{eq}(\mathbf{x}, t) + \epsilon h_i^{(1)}(\mathbf{x}, t) + \epsilon^2 h_i^{(2)}(\mathbf{x}, t), \tag{A.5}$$

Table B.1
Parameters conserved for unit conversion.

Physical quantity	Value in SI units	Value in LBM units
Droplet radius (R)	3×10^{-3} m	20.0
Kinematic viscosity (ν)	1×10^{-6} m^2/s	1.0
Density (ρ)	1000 kg/m^3	1.0
Electrical conductivity (σ)	1×10^{-6} S/m	1.0

$$\nabla = \epsilon \nabla_1, \tag{A.6}$$

where ϵ is a small parameter. On substituting Eqs. (A.4)–(A.6) into Eq. (A.2) and comparing the coefficients of ϵ and ϵ^2, we have

$$(\mathbf{e}_i \cdot \nabla_1) h_i^{eq}(\mathbf{x}, t) = \frac{-1}{\tau_h \delta t}\epsilon h_i^{(1)}(\mathbf{x}, t), \tag{A.7}$$

and

$$\frac{\partial h_i^{eq}(\mathbf{x}, t)}{\partial t_2} + (\mathbf{e}_i \cdot \nabla_1) h_i^{(1)}(\mathbf{x}, t) + \frac{\delta t}{2}(\mathbf{e}_i \cdot \nabla_1)^2 h_i^{eq}(\mathbf{x}, t) = \frac{-1}{\tau_h \delta t} h_i^{(2)}(\mathbf{x}, t). \tag{A.8}$$

Using Eq. (A.7), Eq. (A.8) can be written as

$$\frac{\partial h_i^{eq}(\mathbf{x}, t)}{\partial t_2} + (\mathbf{e}_i \cdot \nabla_1)[(-\tau_h \delta t)(\mathbf{e}_i \cdot \nabla_1) h_i^{eq}(\mathbf{x}, t)] + \frac{\delta t}{2}(\mathbf{e}_i \cdot \nabla_1)^2 h_i^{eq}(\mathbf{x}, t) = \frac{-1}{\tau_h \delta t} h_i^{(2)}(\mathbf{x}, t). \tag{A.9}$$

Using $h_i^{eq} = w_i U$ (Eq. (37)) and taking summation on both sides of Eq. (A.9), we have

$$\frac{\partial U(\mathbf{x}, t)}{\partial t_2} - \nabla_1 \left(\frac{e^2 \delta t}{3}(\tau_h - 0.5)\left(\nabla_1 \left(U(\mathbf{x}, t)\right)\right) \right) = 0. \tag{A.10}$$

In Eq. (A.10), $e^2 \delta t(\tau_h - 0.5)/3$ is considered as the non-dimensional electrical conductivity. Thus, at steady state Eq. (A.10) reduces to the macroscopic equation

$$\nabla \cdot (\sigma \nabla U) = 0. \tag{A.11}$$

Appendix B

Dimensional analysis was done to relate the length, mass, time and electric potential in physical units to LBM units. The physical constants used for the conversion are droplet radius, density, kinematic viscosity and electrical conductivity. For DI water, the parameters used for conversion of physical quantities into lattice parameters are listed in Table B.1.

This gives the dimensional scaling factors as length $C_L = 1.5 \times 10^{-4}$ m, time $C_T = 2.25 \times 10^{-2}$ s, mass $C_M = 3.375 \times 10^{-9}$ kg and voltage $C_V = 5$ V.

References

[1] D. Saville, Electrohydrodynamics: the Taylor-Melcher leaky dielectric model, Annu. Rev. Fluid Mech. 29 (1) (1997) 27–64.
[2] A. Castellanos, A. Ramos, A. Gonzalez, N.G. Green, H. Morgan, Electrohydrodynamics and dielectrophoresis in microsystems: scaling laws, J. Phys. D Appl. Phys. 36 (20) (2003) 2584.
[3] J.-W. Ha, S.-M. Yang, Deformation and breakup of Newtonian and non-Newtonian conducting drops in an electric field, J. Fluid Mech. 405 (2000) 131–156.
[4] K. Ptasinski, P. Kerkhof, Electric field driven separations: phenomena and applications, Separ. Sci. Technol. 27 (8–9) (1992) 995–1021.
[5] M.T. Harris, O.A. Basaran, Capillary electrohydrostatics of conducting drops hanging from a nozzle in an electric field, J. Colloid Interface Sci. 161 (2) (1993) 389–413.

[6] J. Baygents, N. Rivette, H. Stone, Electrohydrodynamic deformation and interaction of drop pairs, J. Fluid Mech. 368 (1998) 359–375.
[7] R. Allan, S. Mason, Particle behaviour in shear and electric fields. I. Deformation and burst of fluid drops, Proc. R. Soc. Lond. Ser. A Math. Phys. Eng. Sci. 267 (1328) (1962) 45–61.
[8] G. Taylor, Studies in electrohydrodynamics. I. The circulation produced in a drop by electrical field, Proc. R. Soc. Lond. Ser. A Math. Phys. Eng. Sci. 291 (1425) (1966).
[9] O.A. Basaran, Small-scale free surface flows with breakup: Drop formation and emerging applications, AIChE J. 48 (9) (2002) 1842–1848.
[10] S. Mhatre, S. Deshmukh, R.M. Thaokar, Electrocoalescence of a drop pair, Phys. Fluids 27 (9) (2015) 092106.
[11] J. Melcher, G. Taylor, Electrohydrodynamics: a review of the role of interfacial shear stresses, Annu. Rev. Fluid Mech. 1 (1) (1969) 111–146.
[12] G. Taylor, Disintegration of water drops in an electric field, Proc. R. Soc. Lond. Ser. A Math. Phys. Eng. Sci. 280 (1382) (1964) 383–397.
[13] S. Torza, R. Cox, S. Mason, Electrohydrodynamic deformation and burst of liquid drops, Proc. R. Soc. Lond. Ser. A Math. Phys. Eng. Sci. 269 (1198) (1971) 295–319.
[14] K. Cheng, J. Chaddock, Deformation and stability of drops and bubbles in an electric field, Phys. Lett. A 106 (1–2) (1984) 51–53.
[15] J.Q. Feng, A 2D electrohydrodynamic model for electrorotation of fluid drops, J. Colloid Interface Sci. 246 (1) (2002) 112–121.
[16] A. Fernández, G. Tryggvason, J. Che, S.L. Ceccio, The effects of electrostatic forces on the distribution of drops in a channel flow: Two-dimensional oblate drops, Phys. Fluids 17 (9) (2005) 093302.
[17] E. Bjørklund, The level-set method applied to droplet dynamics in the presence of an electric field, Comput. Fluids 38 (2) (2009) 358–369.
[18] G. Tomar, D. Gerlach, G. Biswas, N. Alleborn, A. Sharma, F. Durst, S.W. Welch, A. Delgado, Two-phase electrohydrodynamic simulations using a volume-of-fluid approach, J. Comput. Phys. 227 (2) (2007) 1267–1285.
[19] J. López-Herrera, S. Popinet, M. Herrada, A charge-conservative approach for simulating electrohydrodynamic two-phase flows using volume-of-fluid, J. Comput. Phys. 230 (5) (2011) 1939–1955.
[20] M. Herrada, J. L'øpez-Herrera, A.M. Gañán-Calvo, E. Vega, J. Montanero, S. Popinet, Numerical simulation of electrospray in the cone-jet mode, Phys. Rev. E 86 (2) (2012) 026305.
[21] S. Popinet, Gerris: a tree-based adaptive solver for the incompressible Euler equations in complex geometries, J. Comput. Phys. 190 (2) (2003) 572–600.
[22] W.-F. Hu, M.-C. Lai, Y.-N. Young, A hybrid immersed boundary and immersed interface method for electrohydrodynamic simulations, J. Comput. Phys. 282 (2015) 47–61.
[23] E. Lac, G. Homsy, Axisymmetric deformation and stability of a viscous drop in a steady electric field, J. Fluid Mech. 590 (2007) 239–264.
[24] J. Sherwood, Breakup of fluid droplets in electric and magnetic fields, J. Fluid Mech. 188 (1988) 133–146.
[25] S. Succi, The Lattice Boltzmann Equation: for Fluid Dynamics and Beyond, Oxford university press, 2001.
[26] S. Chen, G.D. Doolen, Lattice Boltzmann method for fluid flows, Annu. Rev. Fluid Mech. 30 (1) (1998) 329–364.
[27] J. Zhang, D.Y. Kwok, A 2D lattice Boltzmann study on electrohydrodynamic drop deformation with the leaky dielectric theory, J. Comput. Phys. 206 (1) (2005) 150–161.
[28] X. Shan, H. Chen, Lattice Boltzmann model for simulating flows with multiple phases and components, Phys. Rev. E 47 (3) (1993) 1815.
[29] X. He, N. Li, Lattice Boltzmann simulation of electrochemical systems, Comput. Phys. Comm. 129 (1–3) (2000) 158–166.
[30] Z. Li, G. Li, H. Huang, X. Lu, Lattice Boltzmann study of electrohydrodynamic drop deformation with large density ratio, Internat. J. Modern Phys. C 22 (07) (2011) 729–744.
[31] A. Gupta, R. Kumar, Effect of geometry on droplet formation in the squeezing regime in a microfluidic T-junction, Microfluid. Nanofluid. 8 (6) (2010) 799–812.
[32] D.J. Griffiths, Introduction to Electrodynamics, Pearson Education, 2005.
[33] A. Ramos, Electrokinetics and Electrohydrodynamics in Microsystems, Springer, 2011.
[34] R.P. Feynman, in: Richard P. Feynman, Robert B. Leighton, Matthew. Sands (Eds.), Feynman Lectures on Physics. Volume 2: Mainly Electromagnetism and Matter, Addison-Wesley, Reading, Ma, 1964.
[35] A.K. Gunstensen, D.H. Rothman, S. Zaleski, G. Zanetti, Lattice Boltzmann model of immiscible fluids, Phys. Rev. A 43 (8) (1991) 4320.
[36] S. Lishchuk, C. Care, I. Halliday, Lattice Boltzmann algorithm for surface tension with greatly reduced microcurrents, Phys. Rev. E 67 (3) (2003) 036701.
[37] S. Kondaraju, H. Farhat, J.S. Lee, Study of aggregational characteristics of emulsions on their rheological properties using the lattice Boltzmann approach, Soft Matter 8 (5) (2012) 1374–1384.
[38] H. Liu, Y. Zhang, Droplet formation in microfluidic cross-junctions, Phys. Fluids 23 (8) (2011) 082101.
[39] S. Anwar, Lattice Boltzmann modeling of buoyant rise of single and multiple bubbles, Comput. Fluids 88 (2013) 430–439.
[40] Z. Guo, C. Zheng, B. Shi, Discrete lattice effects on the forcing term in the lattice Boltzmann method, Phys. Rev. E 65 (4) (2002) 046308.
[41] M. Latva-Kokko, D.H. Rothman, Diffusion properties of gradient-based lattice Boltzmann models of immiscible fluids, Phys. Rev. E 71 (5) (2005) 056702.
[42] A. Gupta, R. Kumar, Flow regime transition at high capillary numbers in a microfluidic T-junction: Viscosity contrast and geometry effect, Phys. Fluids 22 (12) (2010) 122001.
[43] D.V. Patil, K.N. Premnath, S. Banerjee, Multigrid lattice Boltzmann method for accelerated solution of elliptic equations, J. Comput. Phys. 265 (2014) 172–194.
[44] J.Q. Feng, Electrohydrodynamic behaviour of a drop subjected to a steady uniform electric field at finite electric Reynolds number, Proc. R. Soc. Lond. Ser. A Math. Phys. Eng. Sci. 455 (1986) (1999) 2245–2269.
[45] J.-W. Ha, S.-M. Yang, Electrohydrodynamics and electrorotation of a drop with fluid less conductive than that of the ambient fluid, Phys. Fluids 12 (4) (2000) 764–772.
[46] J.Q. Feng, T.C. Scott, A computational analysis of electrohydrodynamics of a leaky dielectric drop in an electric field, J. Fluid Mech. 311 (1996) 289–326.
[47] S. Santra, S. Mandal, S. Chakraborty, Electrohydrodynamics of confined two-dimensional liquid droplets in uniform electric field, Phys. Fluids 30 (6) (2018) 062003.
[48] S. Mählmann, D.T. Papageorgiou, Numerical study of electric field effects on the deformation of two-dimensional liquid drops in simple shear flow at arbitrary Reynolds number, J. Fluid Mech. 626 (2009) 367–393.
[49] A. Vananroye, P. Van Puyvelde, P. Moldenaers, Effect of confinement on the steady-state behavior of single droplets during shear flow, J. Rheol. 51 (1) (2007) 139–153.
[50] P. Janssen, A. Vananroye, P. Van Puyvelde, P. Moldenaers, P. Anderson, Generalized behavior of the breakup of viscous drops in confinements, J. Rheol. 54 (5) (2010) 1047–1060.
[51] H.P. Grace, Dispersion phenomena in high viscosity immiscible fluid systems and application of static mixers as dispersion devices in such systems, Chem. Eng. Commun. 14 (3–6) (1982) 225–277.
[52] H. Liu, A.J. Valocchi, Q. Kang, Three-dimensional lattice Boltzmann model for immiscible two-phase flow simulations, Phys. Rev. E 85 (4) (2012) 046309.
[53] J.D. Wehking, L. Chew, R. Kumar, Droplet deformation and manipulation in an electrified microfluidic channel, Appl. Phys. Lett. 103 (5) (2013) 054101.
[54] J.D. Wehking, R. Kumar, Droplet actuation in an electrified microfluidic network, Lab Chip 15 (3) (2015) 793–801.
[55] O. Ozen, N. Aubry, D. Papageorgiou, P. Petropoulos, Monodisperse drop formation in square microchannels, Phys. Rev. Lett. 96 (14) (2006) 144501.
[56] H. Kim, D. Luo, D. Link, D.A. Weitz, M. Marquez, Z. Cheng, Controlled production of emulsion drops using an electric field in a flow-focusing microfluidic device, Appl. Phys. Lett. 91 (13) (2007) 133106.
[57] K. Ahn, C. Kerbage, T.P. Hunt, R. Westervelt, D.R. Link, D. Weitz, Dielectrophoretic manipulation of drops for high-speed microfluidic sorting devices, Appl. Phys. Lett. 88 (2) (2006) 024104.
[58] S. Ponce Dawson, S. Chen, G.D. Doolen, Lattice Boltzmann computations for reaction-diffusion equations, J. Chem. Phys. 98 (2) (1993) 1514–1523.